Cell Reports

Article

Neural manifolds in V1 change with top-down signals from V4 targeting the foveal region

Graphical abstract

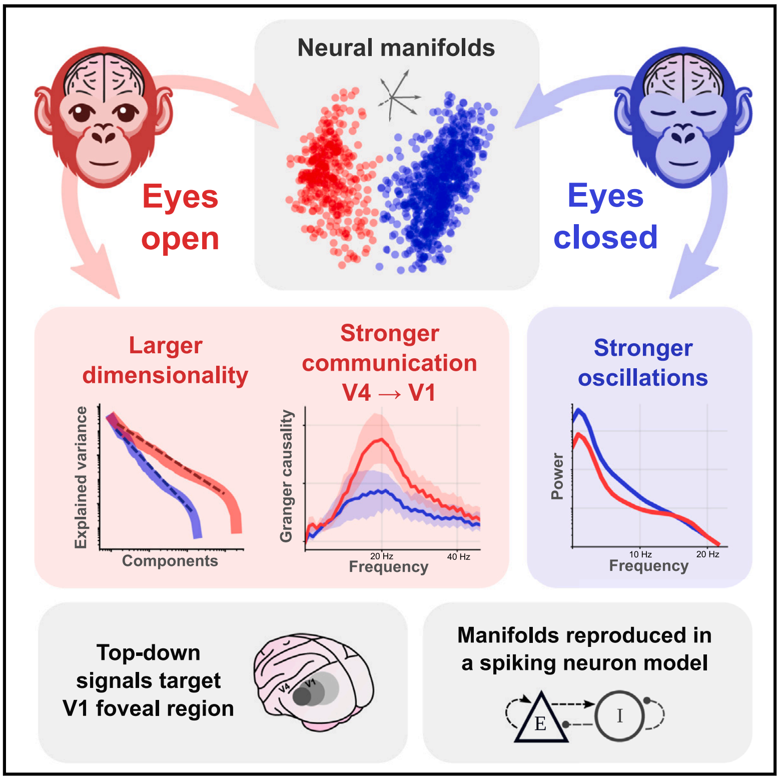

Highlights

- The activity of V1 has two neural manifolds corresponding to the eyes being open or closed
- The dimensionality of the neural data is higher when the eyes are open
- Cortico-cortical communication from V4 to V1 is stronger when the eyes are open
- A computational model shows that the V4 to V1 signals could explain these findings

Authors

Aitor Morales-Gregorio, Anno C. Kurth, Junji Ito, ..., Thomas Brochier, Sonja Grün, Sacha J. van Albada

Correspondence

a.morales-gregorio@fz-juelich.com

In brief

The coordinated activity of many neurons in the brain can be described as a high-dimensional manifold. Morales-Gregorio et al. show that two manifolds appear in the visual cortex of macaques corresponding to the eyes being open or closed. These changes are accompanied by an increase in dimensionality and cortico-cortical communication. Taken together, these observations suggest that as soon as the eyes open V1 is prepared for fast and efficient vision, even in a dark room.

Morales-Gregorio et al., 2024, Cell Reports *43*, 114371
July 23, 2024
https://doi.org/10.1016/j.celrep.2024.114371

Cell Reports

CellPress
OPEN ACCESS

Article

Neural manifolds in V1 change with top-down signals from V4 targeting the foveal region

Aitor Morales-Gregorio,[1,2,7,*] Anno C. Kurth,[1,3] Junji Ito,[1] Alexander Kleinjohann,[1,4] Frédéric V. Barthélemy,[1,5] Thomas Brochier,[5] Sonja Grün,[1,4,6] and Sacha J. van Albada[1,2]
[1]Institute for Advanced Simulation (IAS-6), Jülich Research Centre, Jülich, Germany
[2]Institute of Zoology, University of Cologne, Cologne, Germany
[3]RWTH Aachen University, Aachen, Germany
[4]Theoretical Systems Neurobiology, RWTH Aachen University, Aachen, Germany
[5]Institut de Neurosciences de la Timone (INT), CNRS and Aix-Marseille Université, Marseille, France
[6]JARA-Institut Brain Structure-Function Relationships (INM-10), Jülich Research Centre, Jülich, Germany
[7]Lead contact
*Correspondence: a.morales-gregorio@fz-juelich.com
https://doi.org/10.1016/j.celrep.2024.114371

SUMMARY

High-dimensional brain activity is often organized into lower-dimensional neural manifolds. However, the neural manifolds of the visual cortex remain understudied. Here, we study large-scale multi-electrode electrophysiological recordings of macaque (*Macaca mulatta*) areas V1, V4, and DP with a high spatiotemporal resolution. We find that the population activity of V1 contains two separate neural manifolds, which correlate strongly with eye closure (eyes open/closed) and have distinct dimensionalities. Moreover, we find strong top-down signals from V4 to V1, particularly to the foveal region of V1, which are significantly stronger during the eyes-open periods. Finally, *in silico* simulations of a balanced spiking neuron network qualitatively reproduce the experimental findings. Taken together, our analyses and simulations suggest that top-down signals modulate the population activity of V1. We postulate that the top-down modulation during the eyes-open periods prepares V1 for fast and efficient visual responses, resulting in a type of visual stand-by state.

INTRODUCTION

The brain can be described as a high-dimensional dynamical system capable of representing and processing a plethora of low-dimensional variables.

The time-resolved activity of a population of neurons can be considered as a trajectory in a high-dimensional space, where each neuron represents one dimension, i.e., the state space of the neural system. Typically, the system does not attain all possible states in the state space but rather remains confined to small subsets. These subsets of the state space are referred to as neural manifolds.[1–5] Neural manifolds have been shown to encode aspects such as decision-making in the prefrontal cortex of macaque,[6] hand movement trajectories in the motor cortex of macaque,[2,3,7] odor in the piriform cortex of mice,[8] head direction in the anterodorsal thalamic nucleus of mice,[5] and spatial position in the hippocampus of mice.[9] The study of neural manifolds in the visual cortex has been conducted in mice,[10,11] macaque population,[12] and macaque complex single-neuron[13] visual responses. However, to the best of our knowledge, the state dependence of neural manifolds in the primary visual cortex (V1) of macaque has not yet been investigated.

Neural manifolds often have an intricate structure, which can be studied using methods borrowed from computational topology.[5,12,14] In addition to the topology, the number of uncorrelated covariates required to capture the variance in the state space is studied as a measure of the dimensionality of a neural system.[1,10,15–20] Regardless of species and brain area, the dimensionality is drastically lower than the total number of recorded neurons (i.e., state-space dimension),[1] suggesting robust encoding of low-dimensional variables. Stringer et al.[10] showed that the dimensionality of visual cortical activity in mice can vary dynamically to encode precise visual input, seen as changes in the power law exponent of the explained variance. Such dynamical changes in dimensionality have not yet been demonstrated in other species.

Whether a subject has its eyes open or closed is known to affect the activity in the visual cortex, even in darkness.[21–25] In particular, the spectral power in the alpha frequency band (roughly 8–12 Hz) is known to decrease when the eyes are open, commonly known as alpha blocking.[26–28] Alpha blocking is usually attributed to desynchronization[27] or oscillatory damping[28] within V1. However, the concrete pathway(s) triggering these phenomena, and the relation between eye closure and neural manifolds in V1, are still unknown.

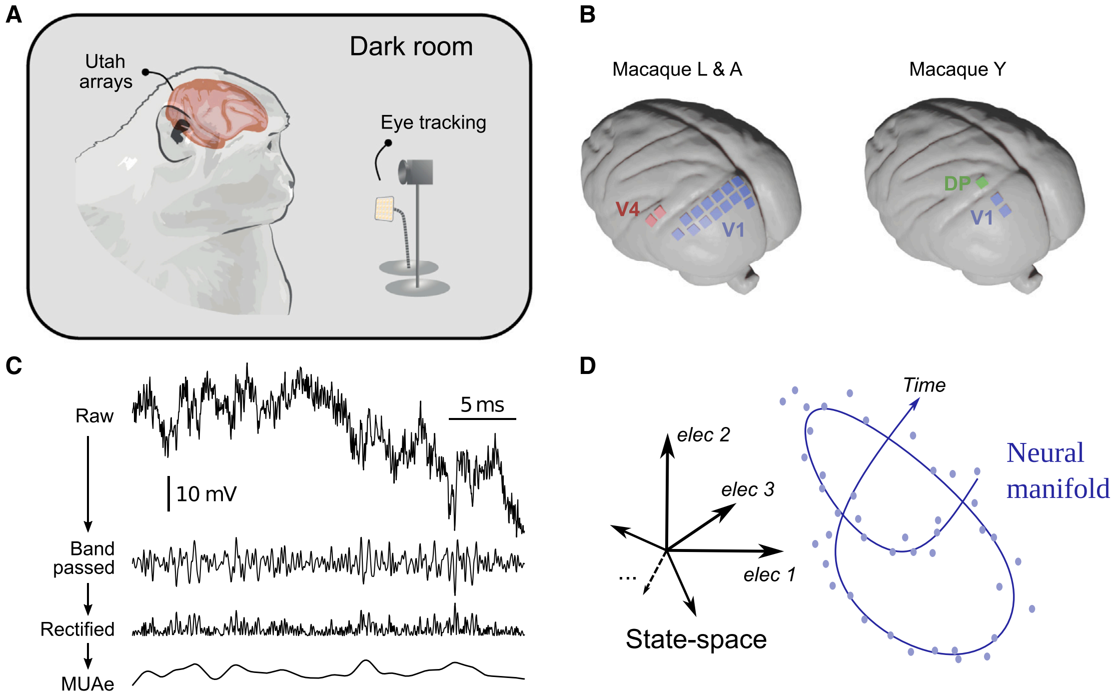

Figure 1. Overview of the experiment and neural manifold construction

(A) Illustration of the experimental setup.

(B) Approximate locations of array implants in both experiments. Exact placement of the arrays differs slightly between subjects L and A.

(C) Steps for obtaining the multi-unit activity envelope (MUAe)[43] used in this study. Band-pass filtering is performed between 500 Hz and 9 kHz, and the rectified signal is low-passed at 200 Hz to obtain the MUAe.

(D) Schematic representation of state space and a neural manifold. Note that time is implicit within the neural manifold.

V1 neurons are known to represent fine details of visual input at both single-neuron and population levels.[12,29] The visual system is hierarchical in nature, with information traveling from lower to higher areas (bottom-up) and vice versa (top-down), within specific frequency bands.[30–33] Top-down signals from V4 to V1 are known to mediate visual attention for figure-ground segregation and contour integration in macaque.[33–37] Recent evidence suggests that top-down signals can modulate neural manifold geometry and dimensionality.[38,39] Naumann et al.[38] show *in silico* that top-down signals can rotate neural manifolds to maintain context-invariant representations. Dahmen et al.[39] show that recurrent connectivity motifs modulate the dimensionality of the cortical activity. As effective connectivity is input dependent,[40] a change in top-down input may therefore affect the dimensionality of neural activity. However, whether top-down signals modulate neural manifold geometry and dimensionality *in vivo* remains to be shown.

Here, we study the state space of the primary visual cortex of the macaque ($n = 3$) during the resting state and its relation to the top-down signals from higher visual areas (V4, DP). We find that the population activity of macaque V1 is organized as two distinct high-dimensional neural manifolds, which are correlated with the behavior (eye closure) of the macaques but not related to specific visual stimuli. The dimensionality of each of these manifolds is significantly different, with higher dimensionality found during the eyes-open periods than the eyes-closed periods. In addition, we estimate input from higher cortical areas to V1 and find that these top-down signals are significantly stronger during the eyes-open periods, suggesting they play a role in modulating the neural manifolds and the dimensionality. Finally, we simulate a spiking neuron model under resting-state conditions and show that top-down signals can induce multiple manifolds by changing the firing modes of the network. Taken together, the data analysis and simulations show that top-down signals can actively modulate the V1 population activity, leading to two distinct neural manifolds of macaque visual cortical activity.

RESULTS

To explore the activity in the visual cortex, the intracortical electrical potential from the visual cortex of three rhesus macaques (*Macaca mulatta*) was recorded. The experiments simultaneously recorded the activity from V1 and V4 (macaques L and A)[41] and from V1 and DP (macaque Y, see Figure 1B).[42] The recordings were made in the resting state; i.e., the macaques sat head-fixed in a dark room and were not instructed to perform any particular task. In this state, the macaques often showed signs of sleepiness and kept their eyes closed for periods of variable duration. The right eye—contralateral to the site of neural recording—was tracked using an infrared camera, allowing the identification of periods of open or closed eyes. See

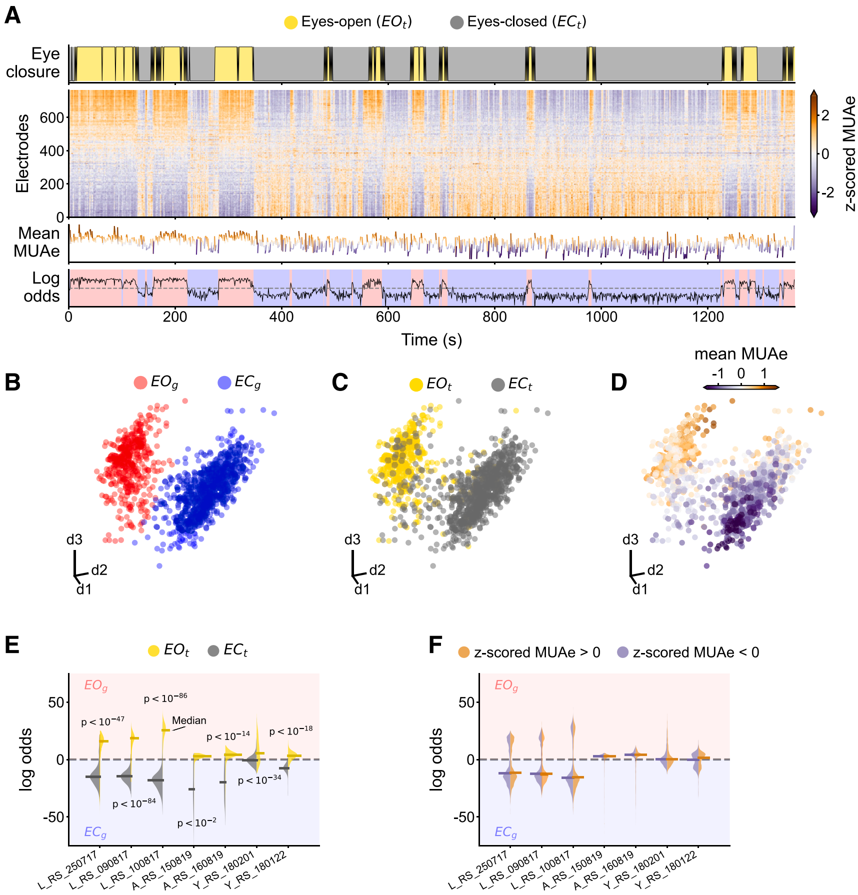

Figure 2. Two distinct neural manifolds in V1 correlated with eye closure

(A) Overview of the experimental data from session L_RS_250717. From top to bottom: time evolution of the eye tracker signal; the *Z*-scored MUAe signal for each electrode (electrodes ordered by their correlation with the eye signal); the mean *Z*-scored MUAe at each time point; and the log odds overlaid with the most likely manifold (two clusters, Gaussian mixture model).

(B–D) The first three principal components of the MUAe population activity. Colors indicate the log odds of a Gaussian mixture (B), the eye tracker signal (C), and the mean *Z*-scored MUAe (D). Each dot represents a different point in time. Outliers were excluded from the neural manifolds shown in (B)–(D) (see "outlier removal").

(E and F) Violin plots of the distribution of the log odds across epochs, distinguished according to the eye tracker signal (E, result of a logistic regression test shown) and *Z*-scored MUAe (F). Horizontal bars indicate medians of the distributions. Note that (D) shows the mean MUAe, whereas (F) shows the full distribution. To distinguish whether the eyes-open (EO) and eyes-closed (EC) periods are estimated from the eye tracker signal or the Gaussian mixture model, we use the subscripts "t" and "g," respectively.

electrophysiological data from macaques L & A and electrophysiological data from macaque Y in STAR Methods for further details on the data acquisition and processing. The experimental setup and data processing steps are illustrated in Figure 1.

Two distinct neural manifolds in V1 correlated with eye closure

We characterize the high-dimensional population activity (between 40 and 800 electrodes, see Table S1 for details) for each area and macaque in terms of the downsampled (1 Hz) multi-unit activity envelope (MUAe)[43] (Figure 2A). We projected the population activity into a 3D space for visualization using principal component analysis (PCA) (Figures 2B–2D).

In V1, at least two distinct neural manifolds are apparent in the 3D projection space (one sample session shown in Figures 2B–2D, see Figures S1–S6 for all other sessions and subjects). We labeled the manifolds according to the sign of the log odds of a two-component Gaussian mixture model (see "neural manifolds and clustering" and "outlier removal". The log odds represent the probability for a given data point to correspond to one manifold or the other.

To confirm that the two manifolds in the lower-dimensional projection are not an artifact of the dimensionality reduction, we estimated the Betti numbers of the high-dimensional population activity using persistent homology (Figure S7). The persistence barcodes show that at least two independent generators of the H_0 homology groups exist in the high-dimensional population activity, corresponding to two connected components (Figure S7), i.e., two distinct neural manifolds. Thus, we confirm that the two manifolds observed in the 3D projection are inherent to the high-dimensional space.

Additionally, we tested whether the observed manifolds could be an artifact of the MUAe signal. We spike-sorted one session (L_RS_250717) with a semi-automatic method and analyzed the population activity resulting from the single-neuron instantaneous firing rates (Figure S8). The spiking activity also displayed two manifolds, in agreement with the MUAe signals.

While the activity of visual cortex is mainly driven by visual input, whether and to what extent it is separately modulated by eye closure are unclear. Marking data points on the V1 manifolds with the eye tracker signal (Figure 2B) reveals that one manifold strongly relates to the eyes-open (EO_t) periods, whereas the other manifold strongly relates to the eyes-closed (EC_t) periods. We use the subscript "t" to refer to the eye closure estimated from the eye-tracking camera.

To confirm the correlation between eye closure and manifolds, we tested the differences between the EO_t and EC_t periods using a 2-fold approach. First, we performed a logistic regression of the eye tracker signal by the log odds, revealing a significantly higher than chance correspondence in all sessions (Figure 2E). Second, we visualized the distribution of the log odds in EO_t and EC_t periods separately, showing a clear correspondence between the eye tracker signal and the sign of the log odds in most cases (Figure 2E). Taken together, the logistic regression and the log odds distributions demonstrate that membership of a point in state space in one of the two V1 manifolds is closely related to eye closure.

Furthermore, we define the EO_g and EC_g periods as the times with a positive or negative Gaussian mixture model log odds (subscript "g" for Gaussian mixture model). Note that EO_t and EO_g periods are very similar, but not identical, likely due to noise from the eye-tracking system. Due to this noise, we consider the Gaussian mixture model log odds to be a more reliable indicator of the eye closure than the eye-tracking camera. Therefore, we consider the EO_g/ EC_g periods to represent the eye closure for the rest of this work.

The existence of two separate manifolds could be trivially explained if the MUAe activity levels were significantly higher in one manifold, and the manifolds simply reflected the mean population activity. To rule out this possibility, we checked whether higher-activity epochs uniquely correspond to one of the manifolds. The violin plots of the full data distribution—based on the *Z*-scored MUAe shown in Figure 2A—show that there is no clear separation into two manifolds (Figure 2F). Additionally, we visualized the 2D histograms of *Z*-scored MUAe against log odds (Figure S9). Both the violin plots and the 2D histograms suggest that the activity level alone does not fully explain the presence of the two neural manifolds in macaque V1.

For completeness, we also visualized the population activity from V4 and DP (Figures S10, and S11). In contrast to V1, the population activity in areas V4 and DP does not appear to contain two distinct neural manifolds. We also tested the relationship between neural activity and eye closure in V4 and DP (Figure S12), using the same procedure as for V1. Although some correlation is observed between the eye tracker signal and log odds, the violins reveal no clear manifold separation. Furthermore, we measured the high-dimensional Euclidean distance between all time points of the MUAe signal, within and across manifolds, as defined from the V1 log odds. The distributions revealed that cross-manifold distances are larger than within-manifold distances in V1 but nearly identical in V4 and DP, quantified by the Wasserstein distance (Figure S13). Thus, we conclude that the observed manifolds are restricted to V1 and are not present in V4 nor DP.

Higher dimensionality during eyes-open periods, primarily due to decorrelation

To further understand the functional role and implications of the observed neural manifolds in V1, we studied the dimensionality in the different conditions (EO_g/ EC_g). We used the participation ratio (PR, Equation 1), which is defined from the eigenvalues of the covariance matrix between the MUAe signals at different electrodes.[19,29] The PR can be rewritten in terms of the statistics of the covariance matrix as

$$\mathrm{PR} = \frac{\left(\sum_i \lambda_i\right)^2}{\sum_i \lambda_i^2} = \frac{N}{1+v^2+(N-1)(m^2+s^2)}, \qquad \text{(Equation 1)}$$

where λ_i are the eigenvalues of the covariance matrix, and N is the number of electrodes. v, m, and s are the ratios between the standard deviation of auto-covariances, average cross-covariances, and the standard deviation of cross-covariances with respect to the average auto-covariances, respectively (see "dimensionality" for detailed methods).

To study the dimensionality, we computed the time-varying PR from the *Z*-scored MUAe signals (Figure 3A) by calculating the PR for 30-s sliding windows (1-s steps, thus 29 s of overlap with adjacent windows). Higher MUAe activity is typically associated with higher variance, which may bias the results toward higher dimensionality. To avoid this bias, we normalize the data via *Z* scoring within each window. We found that there is a strong correlation between the log odds and the time-varying PR (Figure 3B), which we confirmed by comparing the PR values between EO_g and EC_g using a Mann-Whitney U test (Figure 3C). We also measured the PR for one spike-sorted session (Figure S8D). The correlation and statistical tests show that the dimensionality is higher in EO_g periods, consistently for all datasets, both for MUAe and spikes.

To further support this finding, we show the distribution of the variance explained by each of the principal components (PCs) of the MUAe data, depicted on a log-log scale in Figure 3D. Here, we applied PCA separately for EO_g and EC_g periods, unlike in Figure 2, where PCA was applied to the full data. We fitted a power law to the PC variances and report the exponent α (Figure 3E). A higher α indicates faster decay of the curve, i.e., lower dimensionality. The power law exponents are in agreement with our sliding window approach: we observe higher dimensionality in EO_g periods for all sessions (Figure 3E).

To narrow down the reason causing the dimensionality changes, we computed v^2, $(N-1)m^2$, and $(N-1)s^2$ and observed that the changes in $(N-1)m^2$—i.e., the average cross-covariances—dominate the PR differences between EO_g and EC_g periods (Figure 3F). Thus, the main reason for the observed dimensionality changes is decorrelation in EO_g periods.

Top-down signals from V4 to V1 are present in the form of beta-band spectral Granger causality

In search of an internal mechanism that may modulate the neural manifolds and dimensionality, we turned our attention to cortico-cortical interactions. Since signatures of top-down activity have previously been reported in the beta frequency band (roughly 12–30 Hz),[31,33,44] we use spectral Granger causality to measure top-down signals.

To determine whether top-down signals are present in our data, we calculated the coherence and Granger causality between every pair of V1-V4 and V1-DP electrodes (see "coherence and Granger causality") using the local field potential (LFP). Figures 4A and 4B show the coherence and spectral Granger causalities for a sample pair of electrodes. To quantify the cortico-cortical signals, we searched for peaks in the coherence and Granger causality using an automatic method (see peak detection in STAR Methods). We detected beta-frequency Granger causality peaks in a small fraction of all V1-V4 electrode pairs (Figure 4F), predominantly in the top-down direction (see full results in "results from peak detection in LFP coherence and Granger causality" and Table S4). We did not find any gamma-band communication between V1 and V4, a common indicator of bottom-up visual processing,[45] likely

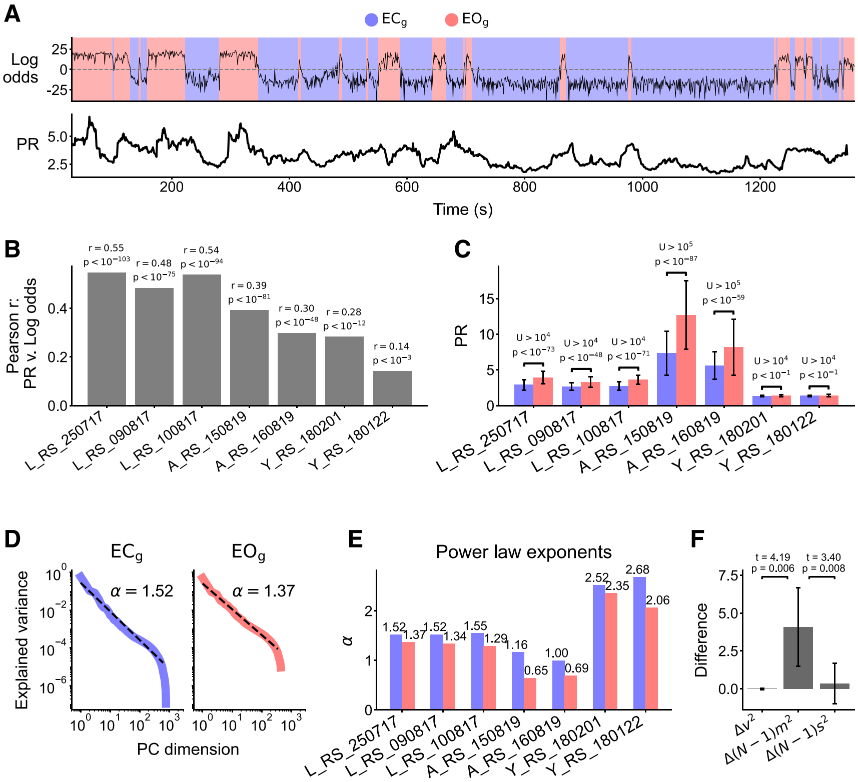

Figure 3. Higher dimensionality in EO_g periods

(A) Log odds and participation ratio (PR) for session L_RS_250717. The PR was calculated on a 30-s sliding window.

(B) Pearson correlation between log odds and PR for each session.

(C) Comparison of PR between neural manifolds (Mann-Whitney U test); error bars indicate the standard deviation.

(D) Distribution of principal components and their explained variance on a log-log scale for each condition. We fit a power law of the form $y = bx^{-\alpha}$, which is linear in the log-log plot since $\log y = -\alpha \log x + \log b$. The power law exponent α was estimated over the ranges where the curves approximate a power law.

(E) Comparison of power law exponents for the two conditions in all sessions. EO_g periods always had a smaller exponent, indicating a higher dimensionality.

(F) Differences in the terms of the PR function between EO_g and EC_g periods; error bars indicate the standard deviation. The results of Welch's t test across sessions are shown. The quantities are related to the standard deviation of auto-covariances (v^2), average cross-covariances ($(N-1)m^2$), and standard deviation of cross-covariances ($(N-1)s^2$).

due to the dark environment. Also, we did not find any communication between V1 and DP.

For the electrodes with a beta causality peak, we estimated the causality strength $\mathcal{B}$ (Equation 6). The electrodes with their visual receptive field (RF) closer to the fovea show substantially higher $\mathcal{B}$ (Figures 4C, 4D, and S17). The communication was restricted to the foveal region, even though the sampling included many pairs with overlapping RFs at different eccentricities (Figure 4D). RFs were approximated as ellipses, and the overlap was measured as the fraction of the V1 RF contained within the V4 RF (Figure S16). The topographic organization of the top-down communication is in agreement with a previous structural connectivity report[46] (Figure 4E).

In conclusion, we found strong top-down signals from V4 to V1, in agreement with previous studies,[31,33,44] but we did not find signals between DP and V1 in our data. V4-to-V1 signals are therefore strong candidates for the modulation of the neural manifolds and dimensionality.

Stronger top-down signals from V4 to V1 during eyes-open periods

To elucidate the behavioral relevance of the V4-to-V1 top-down signals, we examined how the LFP spectral power, coherence, and Granger causality change in relation to eye closure.

We extracted the LFP data for each behavioral condition and concatenated the data within the same condition. This approach could introduce some artifacts, which we expect to be minor in view of the very small number of transitions in comparison with the number of data samples (500-Hz resolution). Both in V4 and V1, we find that the spectral power at low frequencies (<12 Hz) is higher in EC_g periods, whereas the power in the beta band (12–30 Hz) is slightly higher in EO_g periods (Figures 5A and S19). Spectrograms of the V1 LFP power confirm the reduction in low-frequency power in EO_g periods (Figure S21). The coherence in the beta band is higher in EO_g periods, with the peak shifted to higher frequencies compared to EC_g. Notably, the beta-band top-down Granger causality is substantially higher in EO_g periods.

In order to confirm our observations, we also computed the time-dependent spectral Granger causality using a 10-s sliding window (Figure S20A). Statistical tests (Welch's t test) of the time-varying spectral Granger causality confirmed stronger top-down interactions in EO_g compared to EC_g periods for a vast majority of all electrode pairs (Figures S20B and S20C). Thus, we found higher beta-band Granger causality in EO_g periods using two different approaches.

Additionally, to confirm the interdependence of top-down signals and the neural manifolds, we computed the correlation between the time-varying beta-band Granger causality $\mathcal{B}(t)$ (Equation 8) and the log odds (Figures 5B and 5C). An overwhelming majority of V1-V4 electrode pairs showed a highly significant correlation ($p < 10^{-6}$, two-sided t test). Thus, the top-down signals and neural manifolds are co-dependent at a fine temporal scale, regardless of the behavioral condition.

We further tested whether the top-down signals were correlated with gaze direction and eye movements (Figure S22) to rule out the presence of any visual stimuli—despite the experiments being performed in a dark room. No clear trend could

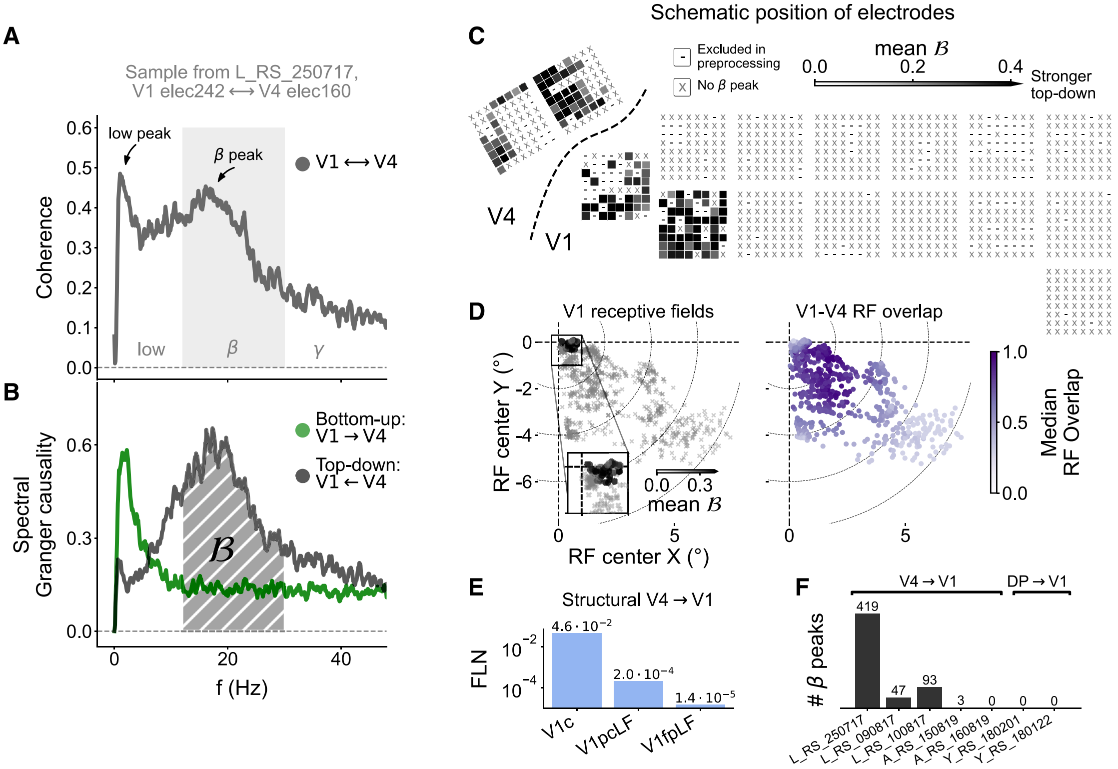

Figure 4. Inter-area coherence and spectral Granger causality

(A) Representative sample of coherence between V1 and V4 (electrodes 242 and 160, respectively). Low-frequency and beta-band peaks are indicated.

(B) Representative sample of spectral Granger causality.

(C) Schematic representation of the electrode locations overlaid with the mean top-down signal strength $\mathcal{B}$ per electrode (see "coherence and Granger causality" for a description of $\mathcal{B}$).

(D) (Left) Receptive field (RF) map overlaid with the mean $\mathcal{B}$ per electrode. Stronger $\mathcal{B}$ is found around the foveal region of V1; the electrodes with no Granger causality peaks in the beta band marked with an x. (Right) Median overlap between V1-V4 RFs, shown on top of the V1 RF centers.

(E) Fraction of labeled neurons (FLN) from V4 to V1 (data from tract-tracing experiments).[46] V1 subdivisions represent c: central (foveal region), LF: lower visual field, pc: peri-central, and fp: far periphery. The strongest connectivity exists from V4 to V1c, in agreement with our measurements.

(F) Number of electrode pairs with strong top-down signals detected in each session.

be observed, thus indicating no relation between gaze direction and top-down signals. This finding suggests that the visual scene is not the source of the observed top-down signals.

The observation of top-down signals particularly in the foveal region (Figure 4) and their correlation with the neural manifolds (Figure 5) suggests that the separation of the neural manifolds should be most prominent around the foveal region. We separated the electrodes from one session (L_RS_250717) into five groups with roughly equal size ($n \approx 140$) based on the distance of their RF center to the fovea (Figure S23). We quantified the EO_g-EC_g differences in mean MUAe, manifold separability, and dimensionality for each group (Figure S23). Around the foveal region ($RFs < 2^\circ$) the observations were compatible with the top-down modulation: small EO_g-EC_g differences in mean MUAe, large separability, and large dimensionality differences. The mid-region ($4^\circ > RFs > 2^\circ$) had small mean MUAe differences, separability, and dimensionality. Interestingly, the periphery ($RFs > 4^\circ$) had large mean MUAe, separability and dimensionality. The observations in the peripheral sites cannot be explained by the top-down modulation and could instead originate from bottom-up interactions. Further research will be needed to fully characterize these central-peripheral differences.

In conclusion, the time-dependent spectral analysis reveals large variations of power and Granger causality. On the one hand, the spectral power at low frequencies decreases in EO_g periods, consistent with the well-known alpha-blocking phenomenon.[26–28] On the other hand, the V4-to-V1 top-down signals are strongest in EO_g periods. The time-varying top-down beta causality strength did not substantially correlate with gaze direction or eye movements, suggesting no relation between the top-down signals and the visual scene—as expected in a dark room. Taken together, these results suggest that V4-to-V1 signals modulate V1 activity, contributing to a different state-space manifold with increased dimensionality, especially in the foveal region.

DISCUSSION

In this paper, we presented three novel findings in the primary visual cortex (V1) of macaques during the resting state: two

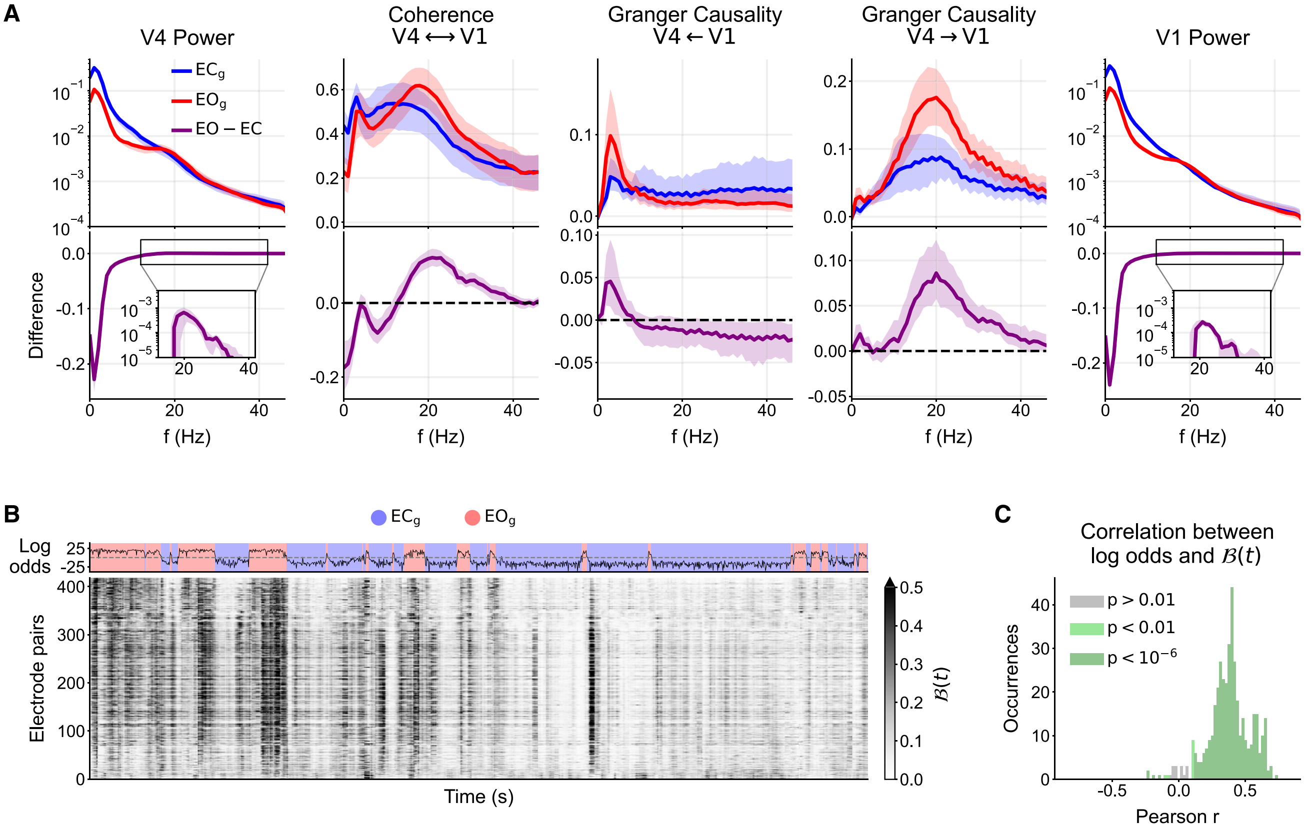

Figure 5. Stronger top-down signals from V4 to V1 in EO_g periods

(A) Spectral power, coherence, and Granger causality of the LFP for the electrodes with Granger causality peaks in session L_RS_250717 (see Figure S19 for all other sessions). The data for each behavioral condition (EO_g/ EC_g) were concatenated and their metrics reported separately (top row). The difference between EO_g and EC_g periods was calculated for each electrode or pair of electrodes (bottom row). In all panels, the thick line shows the median across electrodes (or pairs of electrodes), and shading indicates the 25th to 75th percentile.

(B) Time evolution of log odds (top) and time-dependent beta-band Granger causality strength $\mathcal{B}(t)$ (bottom) for the electrode pairs with top-down signals.

(C) Histogram of the Pearson correlation between the log odds and $\mathcal{B}(t)$. Color indicates the significance levels of the associated two-sided t test.

separate manifolds in the state space associated with eye closure (Figure 2); higher dimensionality due to lower mean cross-correlations in EO_g periods (Figure 3); and the presence of stronger top-down signals from V4 to V1 in EO_g periods, primarily targeting the foveal region of V1 (Figures 4 and 5). In addition, we observed lower power at frequencies below 12 Hz in EO_g periods (Figures 5 and S21), consistent with the well-known alpha-blocking effect.[26]

We observed that two distinct manifolds appear in the state space of macaque V1 during the resting state for all subjects and sessions, for both MUAe and spike data (Figures 2, S1–S6, and S8), and they are correlated with eye closure (Figures 2E and 2F). The manifolds were not just an artifact of the three-dimensional projection used for visualization, as we confirmed they also exist in higher dimensions with persistent homology (Figure S7). The manifolds were not observed in V4 nor DP, in neither the PCA visualization, the Gaussian mixture model, nor the Euclidean distance distributions (Figures S10–S13). Previous work in mice has shown that the visual cortex represents a myriad of behaviors in the resting state, such as facial movements or running.[47] However, a similar study on the macaque showed that the macaque visual cortex is very specific to vision and minimally driven by spontaneous movements.[48] Thus, we do not expect the neural manifolds of V1 to be strongly affected by any behavior other than visual behavior, in agreement with our finding that eye closure neatly explains the two manifolds.

Our findings could in principle be explained by the presence of complex visual stimuli that would alter the population dynamics and cortico-cortical communication. However, we are certain that no strong visual stimuli are present in the visual field, due to the very dark environment of the recording room. Additionally, we performed several analyses to control for activity levels (Figures 2 and S9) and gaze direction (Figure S22). Furthermore, the original data for macaques L and A includes an extensive evaluation of data quality, which excluded all electrodes that did not strongly respond to visual stimuli.[41] Thus, all the electrodes included in our analysis (from macaques L and A) would strongly respond if there were strong visual stimuli, but we observed no such responses in the MUAe activity (see Figure 2). Additionally, we did not find any gamma-band bottom-up interactions between V1 and V4, which would indicate visual processing.[45]

We are therefore certain that the visual input is faint or nonexistent, which implies that the observed neural manifolds must be induced by some internal mechanism.

Further characterization of the activity in the different manifolds revealed that the neural dimensionality is time dependent (Figure 3). We observed higher dimensionality during EO_g periods across all macaques and sessions. Our measured dimensionality is in agreement with previous reports on the visual cortex.[10,16] Previous work has also shown higher dimensionality in EO_g periods in the primary motor cortex,[49] analogous to our findings in the visual cortex. Note that we focused on the dimensionality of the neural activity in terms of number of covariates required to capture a certain amount of the variance. This is fundamentally different from the geometric embedding dimension of the neural manifolds. Nevertheless, the strong correlation between the Gaussian mixture log odds and time-varying PR suggests dimensionality changes are inherent to the underlying manifolds.

We hypothesized that top-down signals from higher cortical areas could be the modulatory mechanism responsible for the changes observed in the neural manifold and dimensionality of V1 activity. Indeed, we found that there are strong top-down signals from V4 to V1 (Figure 4). These signals target particularly the foveal region of V1, in agreement with structural connectivity.[46] We also found the top-down signals to vary over time, with increased presence in EO_g periods (Figure 5). In agreement with our findings, previous studies found that cortico-cortical top-down signals between V1 and V4 are predominantly present in the beta (12–30 Hz) frequency band, while bottom-up signals between V1 and V4 are present in the delta/theta (<8 Hz) and gamma (>30 Hz) bands.[31,44] Others suggest that top-down signals from V4 to V1 are found more generally in the low frequencies (<30 Hz), not uniquely in the beta band.[33] In our analysis we did not find any gamma-band causality (Figure 4), likely because our recordings were from the deep cortical layers (in macaques L and A, the electrodes were 1.5 mm long, likely recording mostly from layer 5), and gamma oscillations are known to be weak in layer 5 of the visual cortex.[30,50] In addition, gamma activity is associated with bottom-up signals,[33,45] which we do not expect in a dark room with no visual stimuli. In contrast to our findings, van Kerkoerle et al.[30] reported that top-down signals appear in the alpha (8–12 Hz) frequency range. Whether the specific top-down and bottom-up frequencies generalize to the whole cortex is unclear. Instead, Vezoli et al.[44] postulate overlapping modules of certain frequencies (alpha, low-beta, high-beta, and gamma) that differ across cortical areas. Our findings are also consistent with the work by Semedo et al.,[51] who suggested that bottom-up signals dominate during visual stimulation and top-down signals dominate in the absence of visual stimuli—note that in their work, the eyes were always open.

The spatial organization of the top-down signals is in agreement with predictions made by the *central-peripheral dichotomy* (CPD) theory.[52,53] In this theory, the central vision is proposed to be primarily concerned with object recognition, and thus, it should be more strongly targeted by top-down inputs (e.g., from V4). These top-down signals would query additional visual information, ultimately reducing ambiguity in visual processing. We also found differences in the separability and dimensionality of the neural manifolds in the center and periphery of V1 (Figure S23), although their link to perception is still unclear.

We did not find top-down signals from DP to V1, possibly due to the electrodes used in macaque Y being 1 mm long, thus likely recording from layer 4, and DP → V1 connections do not originate nor target layer 4.[54] An alternative explanation might be formulated in the context of the CPD theory, which asserts that top-down inputs in the dorsal stream should preferentially target the far periphery of V1,[55] which our experiments did not record from.

In the present study, it was not possible to test directly from the experimental data whether the V4-to-V1 signals are responsible for the modulation of V1 dynamics. Future studies could perform such a test by a reversible inactivation of the V4-to-V1 pathway, such as by reducing the temperature of V4,[56–58] injecting a GABA agonist (e.g., muscimol or bicuculline)[59–61] or using targeted optogenetic suppression.[62] These techniques have been successfully applied to study the suppression of cortico-cortical communication but were not used in our experiments. Therefore, we could not test whether V4-to-V1 signals cause the observed effects in our data. Furthermore, to the best of our knowledge, there are no studies reporting the effects of macaque V4 inactivation in the resting state.

Numerical simulations offer an alternative approach to study whether top-down signals in spiking neural networks can cause distinct neural manifolds. We performed preliminary simulations of a simple spiking neuron model—of the well-known Brunel type[63]—to ascertain whether V4-to-V1 signals can modulate the neural manifolds (Figure 6). Modeled top-down signals, in the form of sinusoidal oscillating inhomogeneous Poisson processes, led to a different neural manifold in the network activity when a subset of the network neurons was targeted (Figure 6D). These changes were not due to the increase in firing rate caused by the additional top-down input but rather due to the activation of different neuron patterns in the model (Figures 6E and 6F). We limited the analysis of the model to the presence of neural manifolds, because our model was ill-suited to study the dimensionality, given that average cross-correlation is known to cancel out in balanced excitatory-inhibitory networks.[64,65] Future work could use more complex models—such as clustered networks[64,66,67]—to study the effects of correlated inputs with realistic power spectra on the dimensionality and elucidate whether the top-down signals can directly induce the observed increase in the dimensionality in EO_g periods.

Taken together, our data analysis and simulations suggest that top-down modulation alone is sufficient to cause the distinct neural manifolds in V1 activity. Nevertheless, sustaining the different V1 manifolds might involve additional mechanisms, such as neuromodulation or adaptation of recurrent connectivity via short-term plasticity. Previous work suggests that N-methyl-D-aspartate (NMDA) receptors are essential for the top-down communication from V4 to V1.[35,68] Interestingly, targeted pharmacological deactivation of NMDA receptors in macaque V1 leads to the suppression of alpha blocking[28] and absence of decorrelation during eyes open,[69] both of which are correlated with the increased V4-to-V1 signals in our data. In addition, the top-down signals are not constant throughout the EO periods (Figure S20), but the slow timescale of the NMDA receptors could

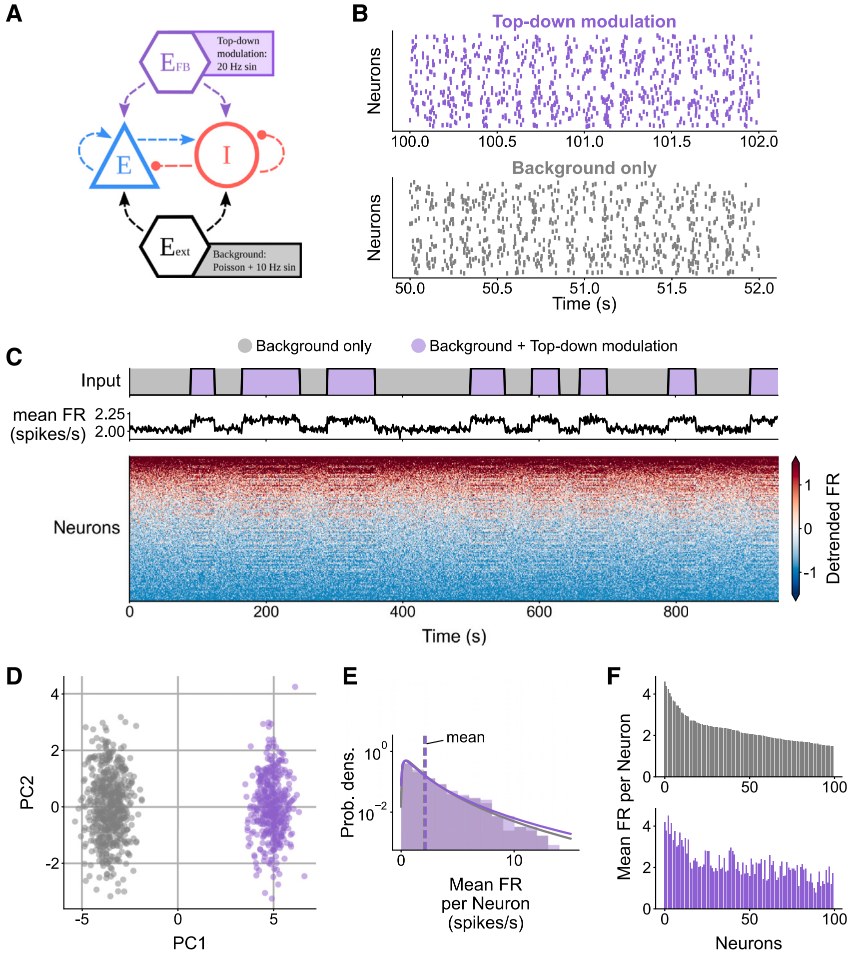

Figure 6. Simulation of a balanced spiking neural network with top-down modulation

(A) Diagram of balanced random spiking neural network. Background input is provided constantly, and top-down signals are provided intermittently.

(B) Sample raster plots show spiking activity in the different input regimes.

(C) Time evolution of input regimes and mean firing rate (FR). Average FRs are 2.026 spikes/s in the background state and 2.164 spikes/s in the top-down input state; the increase is minimal.

(D) First two principal components of the FR (bin size = 1 s). Colors indicate the different input regimes.

(E) Distribution of mean FR per neuron is almost identical between the two regimes. Note the large difference of the plotted scale in (C) and (E).

(F) Mean FR of the 100 most active neurons. The top-down modulation changes the mean FRs of each neuron, in both the positive and negative directions, leading to the observed distinct manifolds.

help sustain the distinct neural manifold during EO periods, even if the top-down input fades. Thus, we speculate that the top-down connections preferentially target the NMDA receptors in V1 neurons, leading to the observed alpha blocking and decorrelation. Another mechanism could involve recurrent connectivity in the form of cell-type-specific motifs. Such motifs have been shown to affect the dimensionality of brain networks,[39] and they could emerge in the effective connectivity of the network as a result of the top-down input.

Saccadic eye movements are known to elicit a biphasic modulation of firing rates (first suppression and then enhancement) in both V1[70] and V4[71] neurons within 100–300 ms after saccade onset. The laminar pattern and latency in V1 suggest lateral geniculate nucleus (LGN) as the source of this modulation, whereas its presence in the dark—although weaker—suggests an extra-retinal origin[70]; the exact pathway is not known. Given the relatively fast timescale (∼100 ms) of post-saccade biphasic modulation, it is unlikely to be the only mechanism affecting our observations of neural manifolds and dimensionality on a slower timescale (1,000 ms). Nevertheless, saccades could trigger other mechanisms leading to the changes on the slower timescales.

If the V4-to-V1 signals convey behavioral information, then how does such behavioral information reach V4 in the first place? We explore the possible communication pathways that lead to the observed V4-to-V1 signals, illustrated in Figure 7. We identified three main candidates: the visual stimulus (or absence thereof) from the retina to V1; the proprioception of eyelid muscles via the somatosensory cortex; and the voluntary motor commands for eye closure. The first proposed pathway involves visual stimuli being transmitted from the retina to V1 via the LGN. The absence of stimuli could be the reason for the observed changes in the V1 activity, whereas the presence of visual stimuli could trigger a V1-V4 feedback loop. However, the macaques in our experiments had very little to no visual input, even when the eyes were open, since they were sitting in a dark room. The eye movements could also contribute to this feedforward pathway from LGN to V1, with their aforementioned biphasic modulation. Another candidate for the modulation is the locus coeruleus (LC), since it innervates the LGN and its activity is known to correlate with arousal.[72,73] However, the LC does not topographically project to the LGN nor V1[72,74] and can therefore not fully explain our observations, especially with respect to the RF eccentricity (Figure S23).

The second proposed pathway involves proprioception of the eyelid that could inform the cortex when the eyes are closed and trigger the activity changes in V1. Mechanoreceptors in the eyelid activate the oculomotor nerve projecting to the midbrain (possibly to the superior colliculus),[75] eventually entering the cortex via the somatosensory area (S1).[76] From S1, the signal could find its way to V1 via several cortico-cortical pathways, potentially including neurons in V4; however, this mechanism might be relatively slow, given the absence of direct connections from S1 to V1 or V4.[77] Furthermore, the shortest known S1-to-V1

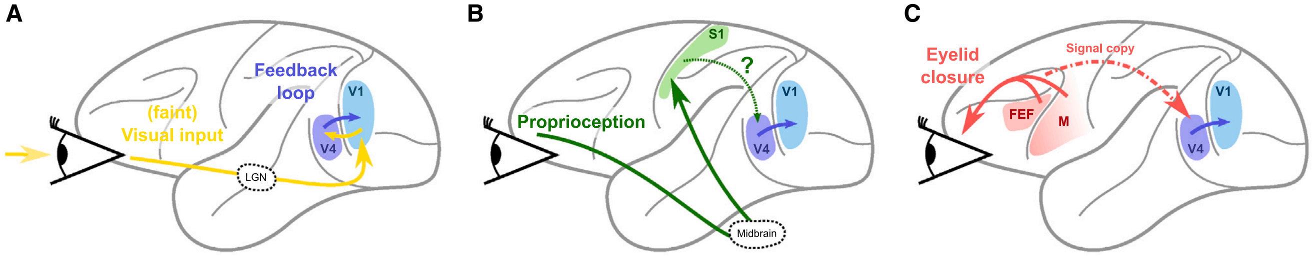

Figure 7. Proposed communication pathways for V1 modulation via V4

(A) Visual input directly to V1 triggering a cortico-cortical feedback loop.

(B) Proprioception of eyelid muscles via the midbrain (possibly superior colliculus) and somatosensory cortex.

(C) Cortico-cortical communication of motor commands.

cortico-cortical pathway does not involve V4, rendering this pathway a rather weak candidate.

The third and final proposed pathway involves voluntary eyelid closure, which is initiated by the ventral motor cortex and the frontal eye field (FEF). The eyelid closure and eye movements may be communicated to the visual cortex via cortico-cortical connections, the superior colliculus, or maybe even the LC. Given that V4 is part of the fronto-parietal network (with strong FEF ⇄ V4 connections),[77,78] the motor signals could easily reach V4, which could then modulate the V1 activity. A trans-thalamic pathway through the pulvinar could also assist the V4-to-V1 communication, including the synchronization of the alpha rhythm,[79] although such trans-thalamic connections have only been confirmed in mice so far.[80]

The hypotheses from Figure 7 are not necessarily mutually exclusive and could all play a role in the modulation of V1 activity, along with other explanations we might have overlooked. To understand which pathways are most relevant to sustain the manifolds, we had a closer look around the manifold transitions (Figure S24) by looking at the MUAe signals at a high temporal resolution (1 kHz). For the eye-opening transitions, we observed that sometimes V1 MUAe activity precedes V4 activity, in agreement with the feedback loop hypothesis (Figure 7A), whereas in other cases, V4 activity precedes V1 activity, in agreement with the motor command hypothesis (Figure 7C). In the eye-closing transitions, the activity from V1 and V4 appeared to be simultaneous. The number of transitions was relatively small, which did not allow for a quantitative analysis of the transitions between the two manifolds. Further work could revisit this issue by looking at longer recordings including larger numbers of transitions between eyes-open and eyes-closed periods.

Given the complex mechanisms that seem to be involved in ensuring that V1 population activity adjusts to eye closure, it seems likely that it has a functional benefit. First of all, if the eyes are closed, no visual stimuli are processed, and V1 firing rates can be reduced to save energy. On the other hand, when the eyes are open, higher-dimensional activity might be advantageous for better encoding visual stimuli, which are known to have a high dimensionality.[10] This could thus facilitate visual processing. Previous work showed that spectral power in the alpha band (8–12 Hz) is inversely correlated with visual recognition performance in human subjects[27,81]; i.e., lower alpha power was associated with better performance in a visual discrimination task. Our results suggest that the change in neural manifolds and dimensionality are directly correlated with the decrease in alpha power (Figures 5 and S21). Future work could study the relation between the dimensionality, alpha power, and visual performance (e.g., response latency to different images) to determine the functional relevance of our findings.

In conclusion, we provide *in vivo* evidence for the modulation of neural manifolds by cortico-cortical communication, which we hypothesize could enable more efficient responses to visual stimuli. Our analysis and previous results suggest that the distinct neural manifold during eyes-open periods—together with the corresponding dimensionality and spectral power changes—constitutes a visual stand-by state, which is modulated by top-down input from V4 and other internal mechanisms.

Limitations of the study

Our study re-analyzes previously published resting-state recordings from the visual cortex,[41] and it is thus fundamentally limited by the original experimental design.

We found that eye closure is related to cortical dynamics (manifolds, dimensionality, and communication), even though the macaques were in a dark room. The actual darkness of the room could not be tested nor adjusted; thus, some visual stimulus in the recording room could in principle trivially explain our observations. We ensure that this is not the case by verifying that there is no direct correlation between gaze direction, activity levels, and communication. Furthermore, we observed no interactions in the LFP gamma band, typically associated with visual input. Therefore, we are confident that our observations are not due to visual stimuli from the room, but rather due to an internal mechanism. Further dedicated experiments, in more strictly controlled darkness, could confirm our findings.

Body movements of the macaques were not tracked, but they could in principle also influence the cortical dynamics. A recent study[48] found that the visual cortex in macaques is minimally driven by movements, strengthening our conclusions.

Another limitation is the small number of subjects and uneven sampling (different areas and electrodes). Originally, we studied $n = 2$ macaques,[41] both of which also participated in visual stimulation experiments[29] (not analyzed here), which could have influenced or damaged the visual cortex in unexpected ways. We thus included recordings from another macaque from a different laboratory,[42] where no visual stimulation was performed, confirming our observations. The two experiments unevenly sampled from different parts of the cortex. We chose to report our results for all three recorded areas (V1, V4, and DP), even when no effects were observed.

The current study could not establish causality between the neural manifolds and cortico-cortical communication. Deactivation of the V4-to-V1 communication pathway would be required to determine whether signals from V4 cause the V1 manifolds. We show in a simple computational model that such top-down signals can in principle be causally related to V1 manifolds. Further experiments will be needed to confirm this link.

STAR★METHODS

Detailed methods are provided in the online version of this paper and include the following:

- KEY RESOURCES TABLE
- RESOURCE AVAILABILITY
  - Lead contact
  - Materials availability
  - Data and code availability
- EXPERIMENTAL MODEL AND STUDY PARTICIPANT DETAILS
  - Macaques
- METHOD DETAILS
  - Electrophysiological data from macaques L & A
  - Electrophysiological data from macaque Y
  - MUAe and LFP signals
  - Spike sorting
- QUANTIFICATION AND STATISTICAL ANALYSIS
  - Neural manifolds and clustering
  - Outlier removal
  - Dimensionality
  - Coherence and Granger causality
  - Peak detection
  - Spiking neural network simulations

SUPPLEMENTAL INFORMATION

Supplemental information can be found online at https://doi.org/10.1016/j.celrep.2024.114371.

ACKNOWLEDGMENTS

We thank David Dahmen for his support with the dimensionality analysis and modeling. We thank Simon Essink, Peter Bouss, and Tobias Kühn for useful feedback about the manifolds and dimensionality. We thank Jon Martinez Corral for proofreading.

This project received funding from the DFG Priority Program (SPP 2041 "Computational Connectomics") (S.J.v.A.: AL 2041/1-1); the EU's Horizon 2020 Framework Grant Agreement No. 945539 (Human Brain Project SGA3); the FLAG-ERA grant PrimCorNet; the Deutsche Forschungsgemeinschaft (DFG, German Research Foundation) 368482240/GRK2416; the NRW-network "iBehave" (grant number NW21-049); and the CNRS Multidisciplinary Exploratory Projects initiative. Open access publication was funded by the Deutsche Forschungsgemeinschaft (DFG, German Research Foundation) 491111487.

AUTHOR CONTRIBUTIONS

A.M.-G., J.I., and A.C.K. conceptualized the study. A.M.-G. curated and processed the data from macaques L and A. A.K. curated and processed the data from macaque Y, with minor inputs from A.M.-G. A.M.-G. and A.C.K. performed the dimensionality analysis, statistical testing, and Granger causality analysis. A.M.-G. wrote the analysis software and workflow, with support from A.C.K. A.C.K. performed the spiking neuron network simulations, and A.M.-G. analyzed the results. A.M.-G. created all figures, with feedback from all other authors. A.M.-G. wrote the initial manuscript; all other authors reviewed the manuscript and provided feedback. J.I., S.G., and S.J.v.A. supervised the project, guiding the scope via active discussions. S.G. and S.J.v.A. procured the funding and provided the necessary resources.

DECLARATION OF INTERESTS

The authors declare that the research was conducted in the absence of any commercial or financial relationships that could be construed as a potential conflict of interest.

Received: September 29, 2023
Revised: March 25, 2024
Accepted: May 31, 2024
Published: June 25, 2024

REFERENCES

1. Gao, P., Trautmann, E., Yu, B., Santhanam, G., Ryu, S., Shenoy, K., and Ganguli, S. (2017). A theory of multineuronal dimensionality, dynamics and measurement. bioRxiv. https://doi.org/10.1101/214262.
2. Gallego, J.A., Perich, M.G., Miller, L.E., and Solla, S.A. (2017). Neural Manifolds for the Control of Movement. Neuron *94*, 978–984.
3. Gallego, J.A., Perich, M.G., Naufel, S.N., Ethier, C., Solla, S.A., and Miller, L.E. (2018). Cortical population activity within a preserved neural manifold underlies multiple motor behaviors. Nat. Commun. *9*, 4233–4313.
4. Feulner, B., and Clopath, C. (2021). Neural manifold under plasticity in a goal driven learning behaviour. A. Morrison, ed. *17*, e1008621.
5. Chaudhuri, R., Gerçek, B., Pandey, B., Peyrache, A., and Fiete, I. (2019). The intrinsic attractor manifold and population dynamics of a canonical cognitive circuit across waking and sleep. Nat. Neurosci. *22*, 1512–1520.
6. Mante, V., Sussillo, D., Shenoy, K.V., and Newsome, W.T. (2013). Context-dependent computation by recurrent dynamics in prefrontal cortex. Nature *503*, 78–84.
7. Churchland, M.M., Cunningham, J.P., Kaufman, M.T., Foster, J.D., Nuyujukian, P., Ryu, S.I., and Shenoy, K.V. (2012). Neural population dynamics during reaching. Nature *487*, 51–56.
8. Wu, A., Pashkovski, S., Datta, S.R., and Pillow, J.W. (2018). Learning a latent manifold of odor representations from neural responses in piriform cortex. In Advances in Neural Information Processing Systems, *31*.
9. Gardner, R.J., Hermansen, E., Pachitariu, M., Burak, Y., Baas, N.A., Dunn, B.A., Moser, M.B., and Moser, E.I. (2022). Toroidal topology of population activity in grid cells. Nature *602*, 123–128.
10. Stringer, C., Pachitariu, M., Steinmetz, N., Carandini, M., and Harris, K.D. (2019). High-dimensional geometry of population responses in visual cortex. Nature *571*, 361–365.
11. Froudarakis, E., Cohen, U., Diamantaki, M., Walker, E.Y., Reimer, J., Berens, P., Sompolinsky, H., and Tolias, A.S. (2020). Object manifold geometry across the mouse cortical visual hierarchy. bioRxiv. https://doi.org/10.1101/2020.08.20.258798.
12. Singh, G., Memoli, F., Ishkhanov, T., Sapiro, G., Carlsson, G., and Ringach, D.L. (2008). Topological analysis of population activity in visual cortex. J. Vis. *8*, 11–18.
13. Baroni, L., Bashiri, M., Willeke, K.F., Antolík, J., and Sinz, F.H. (2022). Learning Invariance Manifolds of Visual Sensory Neurons. NeurIPS.
14. Ghrist, R. (2007). Barcodes: The persistent topology of data. Bull. Amer. Math. Soc. *45*, 61–76.
15. Cunningham, J.P., and Yu, B.M. (2014). Dimensionality reduction for large-scale neural recordings. Nat. Neurosci. *17*, 1500–1509.
16. Gao, P., and Ganguli, S. (2015). On simplicity and complexity in the brave new world of large-scale neuroscience. Curr. Opin. Neurobiol. *32*, 148–155.

17. Pang, R., Lansdell, B.J., and Fairhall, A.L. (2016). Dimensionality reduction in neuroscience. Curr. Biol. *26*, R656–R660.
18. Williamson, R.C., Cowley, B.R., Litwin-Kumar, A., Doiron, B., Kohn, A., Smith, M.A., and Yu, B.M. (2016). Scaling Properties of Dimensionality Reduction for Neural Populations and Network Models. J.W. Pillow, ed. *12*, e1005141.
19. Mazzucato, L., Fontanini, A., and La Camera, G. (2016). Stimuli Reduce the Dimensionality of Cortical Activity. Front. Syst. Neurosci. *10*, 11.
20. Avitan, L., and Stringer, C. (2022). Not so spontaneous: Multi-dimensional representations of behaviors and context in sensory areas. Neuron *110*, 3064–3075.
21. Marx, E., Stephan, T., Nolte, A., Deutschländer, A., Seelos, K.C., Dieterich, M., and Brandt, T. (2003). Eye closure in darkness animates sensory systems. Neuroimage *19*, 924–934.
22. Marx, E., Deutschländer, A., Stephan, T., Dieterich, M., Wiesmann, M., and Brandt, T. (2004). Eyes open and eyes closed as rest conditions: impact on brain activation patterns. Neuroimage *21*, 1818–1824.
23. Boytsova, Y.A., and Danko, S.G. (2010). EEG differences between resting states with eyes open and closed in darkness. Hum. Physiol. *36*, 367–369.
24. McAvoy, M., Larson-Prior, L., Ludwikow, M., Zhang, D., Snyder, A.Z., Gusnard, D.L., Raichle, M.E., and d'Avossa, G. (2012). Dissociated mean and functional connectivity BOLD signals in visual cortex during eyes closed and fixation. J. Neurophysiol. *108*, 2363–2372.
25. Brodoehl, S., Klingner, C.M., and Witte, O.W. (2015). Eye closure enhances dark night perceptions. Sci. Rep. *5*, 10515.
26. Berger, H. (1929). Über das Elektrenkephalogramm des Menschen. Archiv f. Psychiatrie *87*, 527–570.
27. Klimesch, W., Sauseng, P., and Hanslmayr, S. (2007). EEG alpha oscillations: The inhibition-timing hypothesis. Brain Res. Rev. *53*, 63–88.
28. Liley, D.T., and Muthukumaraswamy, S.D. (2020). Evidence that alpha blocking is due to increases in system-level oscillatory damping not neuronal population desynchronisation. Neuroimage *208*, 116408.
29. Chen, X., Wang, F., Fernandez, E., and Roelfsema, P.R. (2020). Shape perception via a high-channel-count neuroprosthesis in monkey visual cortex. Science *370*, 1191–1196.
30. van Kerkoerle, T., Self, M.W., Dagnino, B., Gariel-Mathis, M.A., Poort, J., van der Togt, C., and Roelfsema, P.R. (2014). Alpha and gamma oscillations characterize feedback and feedforward processing in monkey visual cortex. Proc. Natl. Acad. Sci. USA *111*, 14332–14341.
31. Bastos, A.M., Vezoli, J., Bosman, C.A., Schoffelen, J.M., Oostenveld, R., Dowdall, J.R., De Weerd, P., Kennedy, H., and Fries, P. (2015). Visual Areas Exert Feedforward and Feedback Influences through Distinct Frequency Channels. Neuron *85*, 390–401.
32. Klink, P.C., Dagnino, B., Gariel-Mathis, M.A., and Roelfsema, P.R. (2017). Distinct Feedforward and Feedback Effects of Microstimulation in Visual Cortex Reveal Neural Mechanisms of Texture Segregation. Neuron *95*, 209–220.e3.
33. Ferro, D., van Kempen, J., Boyd, M., Panzeri, S., and Thiele, A. (2021). Directed information exchange between cortical layers in macaque V1 and V4 and its modulation by selective attention. Proc. Natl. Acad. Sci. USA *118*, e2022097118.
34. Poort, J., Raudies, F., Wannig, A., Lamme, V.A.F., Neumann, H., and Roelfsema, P.R. (2012). The Role of Attention in Figure-Ground Segregation in Areas V1 and V4 of the Visual Cortex. Neuron *75*, 143–156.
35. Self, M.W., van Kerkoerle, T., Supèr, H., and Roelfsema, P.R. (2013). Distinct Roles of the Cortical Layers of Area V1 in Figure-Ground Segregation. Curr. Biol. *23*, 2121–2129.
36. van Kerkoerle, T., Self, M.W., and Roelfsema, P.R. (2017). Layer-specificity in the effects of attention and working memory on activity in primary visual cortex. Nat. Commun. *8*, 13804.
37. Liang, H., Gong, X., Chen, M., Yan, Y., Li, W., and Gilbert, C.D. (2017). Interactions between feedback and lateral connections in the primary visual cortex. Proc. Natl. Acad. Sci. USA *114*, 8637–8642.
38. Naumann, L.B., Keijser, J., and Sprekeler, H. (2022). Invariant neural subspaces maintained by feedback modulation. Elife *11*, e76096.
39. Dahmen, D., Recanatesi, S., Ocker, G.K., Jia, X., Helias, M., and Shea-Brown, E. (2020). Strong and localized recurrence controls dimensionality of neural activity across brain areas. bioRxiv. https://doi.org/10.1101/2020.11.02.365072.
40. Aertsen, A., and Preissl, H. (1991). Dynamics of activity and connectivity in physiological neuronal networks. Nonlinear Dynamics and Neuronal Networks, 281–301.
41. Chen, X., Morales-Gregorio, A., Sprenger, J., Kleinjohann, A., Sridhar, S., van Albada, S.J., Grün, S., and Roelfsema, P.R. (2022). 1024-channel electrophysiological recordings in macaque V1 and V4 during resting state. Sci. Data *9*, 77.
42. de Haan, M.J., Brochier, T., Grün, S., Riehle, A., and Barthélemy, F.V. (2018). Real-time visuomotor behavior and electrophysiology recording setup for use with humans and monkeys. J. Neurophysiol. *120*, 539–552.
43. Supèr, H., and Roelfsema, P.R. (2005). Chronic multiunit recordings in behaving animals: advantages and limitations. Prog. Brain Res. *147*, 263–282.
44. Vezoli, J., Vinck, M., Bosman, C.A., Bastos, A.M., Lewis, C.M., Kennedy, H., and Fries, P. (2021). Brain rhythms define distinct interaction networks with differential dependence on anatomy. Neuron *109*, 3862–3878.e5.
45. Bosman, C.A., Schoffelen, J.M., Brunet, N., Oostenveld, R., Bastos, A.M., Womelsdorf, T., Rubehn, B., Stieglitz, T., De Weerd, P., and Fries, P. (2012). Attentional Stimulus Selection through Selective Synchronization between Monkey Visual Areas. Neuron *75*, 875–888.
46. Wang, M., Hou, Y., Magrou, L., Autio, J.A., Misery, P., Coalson, T., Reid, E., Xu, Y., Lamy, C., Falchier, A., and Zhang, Q. (2022). Retinotopic organization of feedback projections in primate early visual cortex: implications for active vision. bioRxiv. https://doi.org/10.1101/2022.04.27.489651.
47. Stringer, C., Pachitariu, M., Steinmetz, N., Reddy, C.B., Carandini, M., and Harris, K.D. (2019). Spontaneous behaviors drive multidimensional, brainwide activity. Science *364*, 255.
48. Talluri, B.C., Kang, I., Lazere, A., Quinn, K.R., Kaliss, N., Yates, J.L., Butts, D.A., and Nienborg, H. (2023). Activity in primate visual cortex is minimally driven by spontaneous movements. Nat. Neurosci. *26*, 1953–1959.
49. Dąbrowska, P.A., Voges, N., von Papen, M., Ito, J., Dahmen, D., Riehle, A., Brochier, T., and Grün, S. (2021). On the Complexity of Resting State Spiking Activity in Monkey Motor Cortex. Cerebral Cortex Communications *2*, tgab033.
50. Mendoza-Halliday, D., Major, A.J., Lee, N., Lichtenfeld, M.J., Carlson, B., Mitchell, B., Meng, P.D., Xiong, Y., Westerberg, J.A., Jia, X., et al. (2024). A ubiquitous spectrolaminar motif of local field potential power across the primate cortex. Nat. Neurosci. *27*, 547–560.
51. Semedo, J.D., Jasper, A.I., Zandvakili, A., Krishna, A., Aschner, A., Machens, C.K., Kohn, A., and Yu, B.M. (2022). Feedforward and feedback interactions between visual cortical areas use different population activity patterns. Nat. Commun. *13*, 1099.
52. Zhaoping, L. (2019). A new framework for understanding vision from the perspective of the primary visual cortex. Curr. Opin. Neurobiol. *58*, 1–10.
53. Zhaoping, L. (2023). Peripheral vision is mainly for looking rather than seeing. Neurosci. Res. *201*, 18–26.
54. Markov, N.T., Vezoli, J., Chameau, P., Falchier, A., Quilodran, R., Huissoud, C., Lamy, C., Misery, P., Giroud, P., Ullman, S., et al. (2014). Anatomy of hierarchy: Feedforward and feedback pathways in macaque visual cortex. J. Comp. Neurol. *522*, 225–259.
55. Zhaoping, L. (2023). Peripheral and central sensation: multisensory orienting and recognition across species. Trends Cognit. Sci. *27*, 539–552.
56. Lomber, S.G., Payne, B.R., and Horel, J.A. (1999). The cryoloop: an adaptable reversible cooling deactivation method for behavioral or

electrophysiological assessment of neural function. J. Neurosci. Methods *86*, 179–194.

57. Nassi, J.J., Lomber, S.G., and Born, R.T. (2013). Corticocortical Feedback Contributes to Surround Suppression in V1 of the Alert Primate. J. Neurosci. *33*, 8504–8517.
58. Gómez-Laberge, C., Smolyanskaya, A., Nassi, J.J., Kreiman, G., and Born, R.T. (2016). Bottom-Up and Top-Down Input Augment the Variability of Cortical Neurons. Neuron *91*, 540–547.
59. Dias, E.C., Kiesau, M., and Segraves, M.A. (1995). Acute activation and inactivation of macaque frontal eye field with GABA-related drugs. J. Neurophysiol. *74*, 2744–2748.
60. Brochier, T., Boudreau, M.J., Paré, M., and Smith, A.M. (1999). The effects of muscimol inactivation of small regions of motor and somatosensory cortex on independent finger movements and force control in the precision grip. Exp. Brain Res. *128*, 31–40.
61. Chen, L.L., Goffart, L., and Sparks, D.L. (2001). A simple method for constructing microinjectrodes for reversible inactivation in behaving monkeys. J. Neurosci. Methods *107*, 81–85.
62. Debes, S.R., and Dragoi, V. (2023). Suppressing feedback signals to visual cortex abolishes attentional modulation. Science *379*, 468–473.
63. Brunel, N. (2000). Dynamics of Sparsely Connected Networks of Excitatory and Inhibitory Spiking Neurons. J. Comput. Neurosci. *8*, 183–208.
64. Doiron, B., Litwin-Kumar, A., Rosenbaum, R., Ocker, G.K., and Josić, K. (2016). The mechanics of state-dependent neural correlations. Nat. Neurosci. *19*, 383–393.
65. Tetzlaff, T., Helias, M., Einevoll, G.T., and Diesmann, M. (2012). Decorrelation of Neural-Network Activity by Inhibitory Feedback. N. Brunel, ed. *8*, e1002596.
66. Schaub, M.T., Billeh, Y.N., Anastassiou, C.A., Koch, C., and Barahona, M. (2015). Emergence of Slow-Switching Assemblies in Structured Neuronal Networks. D.S. Bassett, ed. *11*, e1004196.
67. Rostami, V., Rost, T., Riehle, A., Van Albada, S.J., and Nawrot, M.P. (2020). Excitatory and inhibitory motor cortical clusters account for balance, variability, and task performance. bioRxiv. https://doi.org/10.1101/2020.02.27.968339.
68. Van Loon, A.M., Fahrenfort, J.J., van der Velde, B., Lirk, P.B., Vulink, N.C.C., Hollmann, M.W., Scholte, H.S., and Lamme, V.A.F. (2016). NMDA Receptor Antagonist Ketamine Distorts Object Recognition by Reducing Feedback to Early Visual Cortex. Cereb. Cortex *26*, 1986–1996.
69. Herrero, J.L., Gieselmann, M.A., Sanayei, M., and Thiele, A. (2013). Attention-Induced Variance and Noise Correlation Reduction in Macaque V1 Is Mediated by NMDA Receptors. Neuron *78*, 729–739.
70. McFarland, J.M., Bondy, A.G., Saunders, R.C., Cumming, B.G., and Butts, D.A. (2015). Saccadic modulation of stimulus processing in primary visual cortex. Nat. Commun. *6*, 8110.
71. Denagamage, S., Morton, M.P., Hudson, N.V., Reynolds, J.H., Jadi, M.P., and Nandy, A.S. (2023). Laminar mechanisms of saccadic suppression in primate visual cortex. Cell Rep. *42*, 112720.
72. Guillery, R.W., and Sherman, S.M. (2002). Thalamic relay functions and their role in corticocortical communication: generalizations from the visual system. Neuron *33*, 163–175.
73. Joshi, S., Li, Y., Kalwani, R.M., and Gold, J.I. (2016). Relationships between Pupil Diameter and Neuronal Activity in the Locus Coeruleus, Colliculi, and Cingulate Cortex. Neuron *89*, 221–234.
74. Kromer, L., and Moore, R. (1980). A study of the organization of the locus coeruleus projections to the lateral geniculate nuclei in the albino rat. Neuroscience *5*, 255–271.
75. Porter, J.D., Guthrie, B.L., and Sparks, D.L. (1983). Innervation of monkey extraocular muscles: Localization of sensory and motor neurons by retrograde transport of horseradish peroxidase. J. Comp. Neurol. *218*, 208–219.
76. Balslev, D., Albert, N.B., and Miall, C. (2011). Eye muscle proprioception is represented bilaterally in the sensorimotor cortex. Hum. Brain Mapp. *32*, 624–631.
77. Markov, N.T., Ercsey-Ravasz, M.M., Ribeiro Gomes, A.R., Lamy, C., Magrou, L., Vezoli, J., Misery, P., Falchier, A., Quilodran, R., Gariel, M.A., et al. (2014). A Weighted and Directed Interareal Connectivity Matrix for Macaque Cerebral Cortex. Cereb. Cortex *24*, 17–36.
78. Gregoriou, G.G., Gotts, S.J., Zhou, H., and Desimone, R. (2009). High-Frequency, Long-Range Coupling Between Prefrontal and Visual Cortex During Attention. Science *324*, 1207–1210.
79. Lopes da Silva, F.H., Vos, J.E., Mooibroek, J., and Van Rotterdam, A. (1980). Relative contributions of intracortical and thalamo-cortical processes in the generation of alpha rhythms, revealed by partial coherence analysis. Electroencephalogr. Clin. Neurophysiol. *50*, 449–456.
80. Zajzon, B., and Morales-Gregorio, A. (2019). Trans-thalamic Pathways: Strong Candidates for Supporting Communication between Functionally Distinct Cortical Areas. J. Neurosci. *39*, 7034–7036.
81. Hanslmayr, S., Klimesch, W., Sauseng, P., Gruber, W., Doppelmayr, M., Freunberger, R., and Pecherstorfer, T. (2005). Visual discrimination performance is related to decreased alpha amplitude but increased phase locking. Neurosci. Lett. *375*, 64–68.
82. Yger, P., Spampinato, G.L., Esposito, E., Lefebvre, B., Deny, S., Gardella, C., Stimberg, M., Jetter, F., Zeck, G., Picaud, S., et al. (2018). A spike sorting toolbox for up to thousands of electrodes validated with ground truth recordings in vitro and in vivo. Elife *7*, e34518.
83. Dhamala, M., Rangarajan, G., and Ding, M. (2008). Estimating Granger Causality from Fourier and Wavelet Transforms of Time Series Data. Phys. Rev. Lett. *100*, 18701.
84. Wilson, G.T. (1972). The Factorization of Matricial Spectral Densities. SIAM J. Appl. Math. *23*, 420–426.
85. Denker, M., Kern, M., and Richter, F. (2024). Elephant 1.1.0 (v1.1.0). Zenodo. https://doi.org/10.5281/zenodo.10955610.RRID:SCR_003833.
86. Spreizer, S., Mitchell, J., Jordan, J., Wybo, W., Kurth, A., Vennemo, S.B., Pronold, J., Trensch, G., Benelhedi, M.A., Terhorst, D., et al. (2022). NEST 3.3 (3.3). Zenodo. https://doi.org/10.5281/zenodo.6368024.

STAR★METHODS

KEY RESOURCES TABLE

REAGENT or RESOURCE	SOURCE	IDENTIFIER
Deposited data		
Macaque L & A raw data	Chen et al.[41]	doi.gin.g-node.org/10.12751/g-node.i20kyh
Macaque Y raw data	This paper	doi.org/10.5281/zenodo.11204693
Spike sorted data	This paper	doi.org/10.5281/zenodo.11204693
Processed data	This paper	doi.org/10.5281/zenodo.11204693
Experimental models: Organisms/strains		
Macaque monkeys (*Macaca mulatta*)	Netherlands Institute for Neuroscience	L
Macaque monkeys (*Macaca mulatta*)	Netherlands Institute for Neuroscience	A
Macaque monkeys (*Macaca mulatta*)	Institute de Neuroscience de la Timone	Y
Software and algorithms		
Python 3.10.5	Python Software Foundation	www.python.org
nixio 1.5.3	German Neuroinformatics Node	github.com/G-Node/nixpy
neo 0.10.2	NeuralEnsemble	http://neuralensemble.org/neo
odML 1.5.2	German Neuroinformatics Node	g-node.github.io/python-odml
Elephant 0.13.b1	NeuralEnsemble	doi.org/10.5281/zenodo.1186602
Spyking circus	spyking-circus	spyking-circus.rtfd.org
Ripser	scikit-tda	ripser.scikit-tda.org
NEST 3.3	NEST Initiative	nest-simulator.readthedocs.io
SciPy 1.9.3	SciPy Project	scipy.org
Matplotlib 3.8	NumFOCUS	matplotlib.org
Data processing workflow	Custom (Snakemake + Python)	doi.org/10.5281/zenodo.11204693
Spiking neural simulation scripts	Custom (pyNEST)	doi.org/10.5281/zenodo.11204693
Plotting and analysis scripts	Custom (Python)	doi.org/10.5281/zenodo.11204693
Other		
Utah array	Blackrock Microsystems	blackrockneurotech.com/products/utah-array
Omnetics to LGA adapter	Blackrock Microsystems	blackrockneurotech.com
Cereplex M 128 (Macaque L & A)	Blackrock Microsystems	blackrockneurotech.com/products/cereplex-m
Cereplex E (Macaque Y)	Blackrock Microsystems	blackrockneurotech.com/products/cereplex-e
Blackrock Digital Hub 128	Blackrock Microsystems	blackrockneurotech.com
Cerebus Neural Signal Processor	Blackrock Microsystems	blackrockneurotech.com/products/cerebus
Eye tracking system	Thomas Recording GmbH	www.thomasrecording.com/et-49-230hz

RESOURCE AVAILABILITY

Lead contact

Further information and requests for resources should be directed to and will be fulfilled by the lead contact, Aitor Morales-Gregorio (a.morales-gregorio@fz-juelich.de)

Materials availability

This study did not generate new unique reagents.

Data and code availability

- The electrophysiology data from macaques L and A (raw, MUAe, LFP, behavioral) were previously published and are publicly accessible.[41] The electrophysiology data for macaque Y, together with all processed data for this project have been deposited in an online repository and are publicly available at the time of publication under a Creative Commons Attribution-ShareAlike 4.0 International Public License. The DOI to the repository is listed in the key resources table.

- All original code has been deposited at the same repository and is publicly available as of the date of publication. The DOI to the repository is listed in the key resources table.
- Any additional information required to reanalyze the data reported in this paper is available from the lead contact upon request.

EXPERIMENTAL MODEL AND STUDY PARTICIPANT DETAILS

Macaques

We analyzed the resting state data from three ($n = 3$) rhesus macaques (*Macaca mulatta*), recorded in two different experimental laboratories. The data from macaques L & A was collected at the Netherlands Institute for Neuroscience, and previously published.[41] The data from macaque Y was collected at the Institut de Neurosciences de la Timone, with the recording apparatus described elsewhere.[42] At the time of visual cortex array implantation macaque L (male) was 7 years old and weighed 11 kg; macaque A (male) was 7 years old and weighed 12.6 kg; and macaque Y (female) was 6 years old and weighed 7 kg.

All experimental and surgical procedures for Macaque L & A complied with the NIH Guide for Care and Use of Laboratory Animals, and were approved by the institutional animal care and use committee of the Royal Netherlands Academy of Arts and Sciences (approval number AVD-8010020171046).

All experimental and surgical procedures for Macaque Y were approved by the local ethical committee (C2EA 71; authorization Apafis#13894-2018030217116218v4) and conformed to the European and French government regulations.

METHOD DETAILS

Electrophysiological data from macaques L & A

We used publicly available[41] neural activity recorded from the neocortex of rhesus macaques ($n = 2$) during rest and a visual task. The macaques were implanted with 16 Utah arrays (Blackrock microsystems), two of them in visual area V4 and the rest in the primary visual cortex (V1), with a total of 1024 electrodes. The electrodes were 1.5 mm long, thus recording from the deeper layers, likely layer 5. The system recorded the electric potential at each electrode with a sampling rate of 30 kHz. A full description of the experimental setup and the data collection and preprocessing has already been published[41]; here we only provide the details relevant to this study.

Three resting-state (RS) sessions were recorded per macaque, during which the subjects did not have to perform any particular task and sat in a quiet dark room. Pupil position and diameter data were collected using an infrared camera in order to determine the direction of gaze and eye closure of the macaques. On the same days as the RS recordings, a visual response task was also performed. The visual response data were used to calculate the signal-to-noise ratio (SNR) of each electrode, and all electrodes with an SNR lower than 2 were excluded from further analysis. Additionally, we excluded up to 100 electrodes that contributed to high-frequency cross-talk in each session, as reported in the original data publication.[41] The sessions, duration and number of electrodes per subject are listed in Table S1.

Electrophysiological data from macaque Y

In addition to the published data from macaques L & A, we also used an unpublished dataset from one additional rhesus macaque ($n = 1$). Neural activity was recorded during rest and during a visuomotor integration task. The recording apparatus is described elsewhere.[42] Macaque Y was implanted with five Utah arrays (Blackrock microsystems), two of them in the primary visual cortex (V1), one in dorsal prelunate cortex (area DP), one in area 7A and one in the motor cortex (M1/PMd). In this study we only included the 6x6 electrode arrays from V1 (two arrays) and DP (one array), for a total of 108 electrodes. The electrodes were 1 mm long, thus recording from the central layers, likely layer 4. The recording system recorded the electric potential at each electrode with a sampling rate of 30 kHz.

Two resting-state (RS) sessions were recorded, during which the macaque did not have to perform any particular task and sat in a quiet dark room. Pupil position and diameter data were collected using an infrared camera in order to determine the gaze direction and eye closure of the macaque. We excluded up to 50% of the electrodes that contributed to high-frequency cross-talk in each session, similarly to the methods described in.[41] See Table S1 for an overview of the sessions used in this study.

MUAe and LFP signals

The raw neural data were processed into the multi-unit activity envelope (MUAe) signal and local field potential (LFP). To obtain MUAe data, the raw data were high-pass filtered at 500 Hz, rectified, low-pass filtered at 200 Hz, and downsampled to 1 kHz. Finally, the 50, 100, and 150 Hz components were removed with a band-stop filter in order to remove the European electric grid noise and its main harmonics. To obtain the LFP data, the raw data was low-pass filtered at 250 Hz, downsampled to 500 Hz and a band-stop filter was applied to remove the European electric grid noise (50, 100, and 150 Hz).

The MUAe and LFP data for macaques L & A were already provided by the original authors[41] in the open-source.nix format, which uses python-neo data structures to hierarchically organize and annotate electrophysiological data and metadata. The metadata, such as the cross-talk removal or the positions of the arrays in the cortex, were provided in the .odml machine- and human-readable format, which were incorporated into the python analysis scripts.

Spike sorting

The raw data from one session (L_RS_250717) were spike-sorted using a semi-automatic workflow with Spyking Circus—a free, open-source, spike-sorting software written entirely in Python.[82] An extensive description of the methods of this algorithm can be found in their publication, as well as in the online documentation of Spyking Circus (spyking-circus.readthedocs.io).

Roughly, Spyking Circus first applied a band-pass filter to the raw signals between 250 Hz and 5 kHz. Next, the median signal across all 128 channels that shared the same reference (2 Utah arrays) was calculated and subtracted, in order to reduce cross-talk and movement artifacts. The spike threshold was set conservatively, at eight times the standard deviation of each signal. After filtering and thresholding, the resulting multi-unit spike trains were whitened—removing the covariance from periods without spikes to reduce noise and spurious spatiotemporal correlations. After whitening, a subsample of all spike waveforms is selected, reduced to the first five principal components, and clustered into different groups with the k-medians method. Finally, all spikes in each electrode are assigned to one of the waveform clusters based on a template fitting algorithm, which can also resolve overlapping waveforms.

After the automatic sorting, the waveform clusters were manually merged and labeled as single-unit activity, multi-unit activity, or noise. Only single-unit activity (SUA) spike trains were included in this study. The waveform signal-to-noise ratio (wfSNR) was calculated for all SUA, and those with a wfSNR < 2 or electrode SNR < 2 (from the visual response task) were excluded from the analysis.

QUANTIFICATION AND STATISTICAL ANALYSIS

Neural manifolds and clustering

The MUAe data were downsampled to 1 Hz and arranged into a single array, with between 50 and 900 recording locations per session.

In order to visualize the data, we used a standard dimensionality reduction technique (principal component analysis, PCA) to reduce the neural manifold to 3D. The clusters observed in the RS sessions were labeled using a two-component Gaussian mixture model on the 3D projection. The clustering method provides the log odds, i.e., the chance that any given point belongs to one cluster or the other. The log odds captures the multi-cluster structure of the manifold in a single time series; thus, we consider it to be an identifier of the V1 manifolds.

Outlier removal

The neural manifolds in our analysis are a collection of time points scattered across the state space. In the data some time points appear very distant from all other points, which we associate with noise and we therefore seek to remove them. To identify the outliers we used a procedure similar to the one used by Chaudhuri et al.[5] First, we calculated the distance matrix of all points to each other, and took the 1st percentile value from the distance distribution, D_1. We then estimated the number of neighbors that each point had within D_1 distance, and finally discarded the 20 percent of points with the fewest neighbors.

Dimensionality

We used two different approaches to study the dimensionality of the neural data.

First, we compute the time-varying participation ratio (PR, Equation 1) from the covariance matrix. We take a 30-s sliding window with 1 s offset over the MUAe data and compute the PR for each window separately. Higher activity leads to higher variance; thus, we normalized the data within each window via Z-scoring to minimize this effect. The PR does not require setting an arbitrary threshold. From the time-varying PR we measured the correlation between the log odds and the PR, and the PR distribution in each manifold.

Second, we computed the eigenvalue distribution of the neural data within each manifold. Once again we normalized the data after sampling each manifold. The distribution appeared to follow a power law, in agreement with previous studies.[10] We used a linear regression in log-log space to fit a power law to our data, where the slope of the linear fit in the log-log plot corresponds to the exponent α of the power law.

Coherence and Granger causality

To estimate the communication between cortical areas we rely on the coherence and Granger causality of the LFP.

Coherence is the quantification of linear correlations in the frequency domain. Such that,

$$C_{xy}(f) = \frac{\left|S_{xy}(f)\right|^2}{S_{xx}(f)S_{yy}(f)}, \tag{Equation 2}$$

where C_{xy} is the frequency (f) dependent coherence between two signals x and y, $S_{xy}(f)$ is the cross-spectral density, and $S_{xx}(f)$ and $S_{yy}(f)$ are the auto-spectral densities (also known as power-spectra). The cross and auto-spectra are defined as

$$S_{xy}(f) = \mathcal{F}_x(f)\overline{\mathcal{F}_y(f)}, \tag{Equation 3}$$

where $\mathcal{F}_x(f)$ is the Fourier transform of signal x and $\overline{\mathcal{F}_y(f)}$ is the complex conjugate of $\mathcal{F}_y(f)$.

In order to assess the directionality of frequency dependent interactions between the areas we applied spectral Granger causality analysis to the LFP recordings. Spectral Granger causality between two time series x_t, y_t can be given in terms of a parametric multivariate auto-regressive (MVAR) model.[83] We assume

$$x_t = \sum_{j=1}^{p} a_{11}^{j} x_{t-j} + \sum_{j=1}^{p} a_{12}^{j} y_{t-j} + \eta_x$$

$$y_t = \sum_{j=1}^{p} a_{21}^{j} x_{t-j} + \sum_{j=1}^{p} a_{22}^{j} y_{t-j} + \eta_{y,}$$

where η_x, η_y are zero-mean Gaussian noise terms with covariance matrix Σ and p is the order of the MVAR model. We used an approach based on spectral analysis and spectral matrix factorisation.[83] We first computed the cross-spectral matrix $S(f)$ (the diagonal elements of which are $S_{xx}(f)$ and $S_{yy}(f)$ and the off-diagonal elements are $S_{xy}(f)$ and $S_{yx}(f)$) with the multitaper method. Note that by definition $S(f) = S(f)^{\dagger}$ where $\dagger$ denotes the Hermitian conjugate. To this end, we subdivided the chosen signal pairs into 10-s long segments. These were processed individually with 3 Slepian tapers and averaged in the end. This yielded the cross-spectrum. The segments had an overlap of 50%. Next, we decomposed the cross-spectrum into the covariance matrix Σ and the transfer function $H(f)$ with the Wilson spectral matrix factorisation[84]:

$$S(f) = H(f)\Sigma H^{\dagger}(f). \tag{Equation 4}$$

Here, Σ is the covariance matrix of the noise from the MVAR model. The matrix-valued function $H(f)$ can be represented by a function ψ evaluated at e^{if}: $H(f) = \psi(e^{if})$. For these arguments, ψ can be given by an infinite series, $\psi(e^{if}) = \sum_{k=0}^{\infty} B_k e^{ikf}$, where B_k are matrix valued coefficients, and B_0 is required to be the identity matrix. The function ψ is initially only defined on the unit circle $\{z \in \mathbb{C} \| z| = 1\} = \{e^{if} | f \in [0, 2\pi)\}$ but can be extended to a holomorphic function on the disc $\{z \in \mathbb{C} | z| < 1\}$[83]. With these factors, one is able to obtain a version of directional functional connectivity between the first and second signals via

$$\mathrm{GC}_{x \to y}(f) = \frac{S_{xx}(f)}{\tilde{H}_{xx}(f)\Sigma_{xx}\tilde{H}_{xx}^{\dagger}(f)} \tag{Equation 5}$$

where $\tilde{H}_{xx}(f) = H_{xx}(f) + \Sigma_{xy}/\Sigma_{xx}H_{xy}(f)$ and mutatis mutandis for the influence of the second onto the first signal. The analysis was performed for all pairs of channels between the areas that exhibited a peak in the coherence of the corresponding frequency band.

We quantify the Granger causality strength as

$$\mathcal{R} = \frac{1}{f_1 - f_0} \sum_{f_0}^{f_1} \mathrm{GC}_{x \leftarrow y}(f) \tag{Equation 6}$$

where f_0 and f_1 are the edges of the selected frequency band. In this study we use the following bands: l (2–12 Hz), β (12–30 Hz), γ (30–45 Hz), and $\hat{\gamma}$ (55–95 Hz); note the safety margin around the line noise and its harmonics (50 Hz, 100 Hz). The strengths corresponding to each band are denoted by $\mathcal{L}$, $\mathcal{B}$, $\mathcal{G}$, and $\hat{\mathcal{G}}$.

We also analyzed the time-varying spectral Granger causality. For this aim we used 10 s windows and moved them across the data with 1 s steps, for a final time resolution of 1 Hz. We calculated the spectral Granger causality for each window separately. The initial and final 5 s were discarded to avoid disruptions at the boundaries. So the time-varying spectral Granger causality is

$$\mathrm{GC}_{x \leftarrow y}(t, f) = \mathrm{GC}_{x \leftarrow y}(f)|_{[t_0, t_1]}, \ldots, \mathrm{GC}_{x \leftarrow y}(f)|_{[t_{n-1}, t_n]} \tag{Equation 7}$$

and mutatis mutandis for the $x \to y$ direction. From which we define the time-varying strength as

$$\mathcal{R}(t) = \frac{1}{f_1 - f_0} \sum_{f_0}^{f_1} \mathrm{GC}_{x \leftarrow y}(t, f). \tag{Equation 8}$$

Note that

$$\mathcal{R} \neq \frac{\sum_i^N \mathcal{R}(t_i)}{N} \tag{Equation 9}$$

due to the nonlinearities in the Granger causality calculation.

Both the coherence and spectral Granger causality were implemented in the Electrophysiology Analysis Toolkit (Elephant).[85]

Peak detection

To detect coherence and Granger causality peaks (used to identify admissible channel pairs for our analysis) we used a standard peak detection algorithm for 1D arrays. First, we smoothed the coherence and Granger causality with a Ricker wavelet (wavelet with 25 points applied in a window 500 bins wide), to reduce the noise in the signal. Then, we applied a standard algorithm where points that were higher than their immediate neighbors were considered peaks. The prominence of the peaks was automatically determined from their height and width, and peaks with low prominence (less than 0.1) were rejected. The detected peaks tended to be broad, since our parameter choice intentionally rejected narrow and small peaks. We chose this configuration in favor of robustness and to minimize false positives.

We further enforced several constraints to ensure that the detected peaks correspond to real cortico-cortical communication. First, we rejected any peaks that did not appear in both the coherence and the Granger causality. Next, we rejected Granger causality peaks that had a higher instantaneous causality than the directed causality. The instantaneous causality measures the zero-lag co-fluctuations, which cannot reflect unidirectional communication, nor distinguish communication from external common inputs. Then, we rejected peaks with a low strength ($\mathcal{R} < 0.2$) within the corresponding band, as defined in Equation 6. Finally, we visualized all the remaining peaks and manually rejected some surviving false positives.

Some examples of true positive (Figure S14), true negative (Figure S14) and false positive (Figure S15) peak detection are shown in the supplement. The final manual curation step ensured that no false positive results were included in our analysis.

Spiking neural network simulations

To investigate the hypothesis that top-down signals in the β-band induce a change in the population dynamics and dimensionality, we conducted a spiking neural network simulation. The network consists of $10,000$ excitatory and $2,000$ inhibitory leaky integrate-and-fire (LIF) neurons with exponential post-synaptic currents. Pairs of neurons are randomly connected with a connection probability of $p = 0.1$. The spike transmission delay is randomly sampled following a log-normal distribution. Generally speaking, the simulation experiments consist of two parts corresponding to the two states observed in the neuronal activity. In the first state (background state), the input consists of spike trains sampled from an inhomogeneous Poisson process with a baseline rate of ν_{bg} Hz that is modulated with a 1 Hz sinusoidal oscillation. In the second state, the network additionally receives input spike trains from inhomogeneous Poisson processes with rates oscillating at 20 Hz. The first state represents the EC state, the second the EO state. Both input regimes provide independent input to each neuron, based on the same rate profiles. We recorded the spiking activity of $1,000$ excitatory and 200 inhibitory neurons. We provided the top-down modulation to a subset of the neurons in the network. We targeted 50% of both the excitatory and inhibitory population. During the simulation, we distinguish two manifolds, corresponding to the EO and EC periods in the experimental recordings. See Table S2, Table S3 for a full description of the network and the experiments. For the simulations we used NEST (version 3.3).[86]